On Power Control of Grid-Forming Converters: Modeling, Controllability, and Full-State Feedback Design

Chen, Meng; Zhou, Dao; Tayyebi, Ali; Prieto-Araujo, Eduardo; Dörfler, Florian; Blaabjerg, Frede

Published in:
I E E E Transactions on Sustainable Energy

DOI (link to publication from Publisher):
10.1109/TSTE.2023.3271317

Publication date:
2023

Document Version
Accepted author manuscript, peer reviewed version

On Power Control of Grid-Forming Converters: Modeling, Controllability, and Full-State Feedback Design

Meng Chen, *Member, IEEE,* Dao Zhou, *Senior Member, IEEE,* Ali Tayyebi, Eduardo Prieto-Araujo, *Senior Member, IEEE,* Florian Dörfler, *Senior Member, IEEE,* and Frede Blaabjerg, *Fellow, IEEE*

***Abstract*—The popular single-input single-output control structures and classic design methods (e.g., root locus analysis) for the power control of grid-forming converters have limitations in applying to different line characteristics and providing favorable performance. This paper studies the grid-forming converter power loops from the perspective of multi-input multi-output systems. First, the error dynamics associated with power control loops (error-based state-space model) are derived while taking into account the natural dynamical coupling terms of the power converter models. Thereafter, the controllability Gramian of the grid-forming converter power loops is studied. Last, a full-state feedback control design using only the local measurements is applied. By this way, the eigenvalues of the system can be arbitrarily placed in the timescale of power loops based on predefined time-domain specifications. A step-by-step construction and design procedure of the power control of grid-forming converters is also given. The analysis and proposed method are verified by experimental results and system-level simulation comparisons in Matlab/Simulink.**

***Index Terms*—full-state feedback control, grid-forming converter, power control, loop coupling, controllability, line impedance.**

I. Introduction

GRID-FORMING converters are becoming vital to the power systems due to their ability to help stabilize the frequency and voltage. The control architecture of grid-forming converters is typically nested with multiple loops, e.g., inner cascaded voltage and current loops as well as the outer power loops. To simplify the analysis and design, the cascaded loops are usually designed with higher bandwidths than those of the power loops. As a result, the cascaded loops with the fast dynamics and the power loops with the slow dynamics can be studied separately [1].

In terms of the cascaded loops, the conventional structure is with double proportional-plus-integral (PI) controllers. In [2], an additional high-pass filter is added to the current feedback loop to obtain a faster voltage tracking. The sliding-mode control is used to completely replace the PI control for the cascaded loops in [3]. These strategies enhance the decoupling between the inner cascaded loops and the outer power loops.

As for the power controls, several strategies have been proposed, e.g., droop control [4], [5], virtual synchronous generator (VSG) control [6], [7], virtual oscillator control [8], matching control [9], power synchronization control [10], [11], hybrid angle control [12], etc. Until now, the characteristics of these grid-forming controls have been studied from different aspects. In [13] and [14], the transient stability of the grid-forming control is investigated while the analysis of the small-signal stability is carried out in [15]. In [16], how the grid-forming converters can be used to enhance the system-level stability of the power system is theoretically investigated. Besides, several pilot projects have also been carried out to demonstrate the feasibility and effectiveness of the grid-forming control as reviewed in [17]. Beyond those basic strategies, to obtain better performance, various improved grid-forming power controls have been proposed recently. In [18], the virtual reactance is used to dampen the low-frequency resonance of the grid-forming control based on a passivity-based analysis. In [19], two transient damping terms are added into the active power control loop to suppress the active power oscillation. More structures of the improved grid-forming control have been summarized in [20]. Nevertheless, there still are many concerns which are worth studying in detail.

First, the control performance is limited by the line characteristics. Usually, an inductive or resistive line is assumed in the aforementioned controls, where, as a result, the frequency and voltage can be controlled by two decoupled single-input single-output (SISO) loops, e.g., p-f and q-V loops for an inductive line, respectively [21], [22]. However, this decoupled control architecture will inevitably exert additional restraints on both the system and controller parameters [23]. Further, the decoupling is just an approximate rather than exact result. More important, in a complex line, the frequency, voltage, active and reactive powers are tightly coupled with each other, which may lead to large errors and suboptimal dynamics performance when using two SISO control loops. In the literature, two methods have been used to solve this problem. Most usually, a virtual impedance (VI) can be added to enlarge the equivalent inductance [24]. Therefore, the p-f and q-V relationships can still be used for a complex

This work was supported by the Reliable Power Electronic-Based Power System (REPEPS) project at AAU Energy, Aalborg University as part of the Villum Investigator Program funded by the Villum Foundation. (Corresponding author: Meng Chen.)

M. Chen, D. Zhou, and F. Blaabjerg are with the AAU Energy, Aalborg University, 9220 Aalborg, Denmark (e-mail: mche@energy.aau.dk; zda@energy.aau.dk; fbl@energy.aau.dk).

A. Tayyebi is with the Hitachi Energy Research (HER), 72226 Västerås, Sweden, and also with the Automatic Control Laboratory, ETH Zürich, 8092 Zürich, Switzerland (email: ali.tayyebi@hitachienergy.com).

E. P.-Araujo is with the CITCEA-UPC, Technical University of Catalonia, 08028 Barcelona, Spain (email: eduardo.prieto-araujo@upc.edu). He is a lecture of the Serra Húnter programme.

F. Dörfler is with the Automatic Control Laboratory, ETH Zürich, 8092 Zürich, Switzerland (email: dorfler@ethz.ch).

line. Nevertheless, the VI should be designed carefully to obtain favorable stability, performance, and avoid undesired wind-up behavior [25]. Meanwhile, this method is still relies on an approximate decoupling. The other method is to use multi-input multi-output (MIMO) control structures [20], [26], e.g., the MIMO-GFM converter, where no assumption of decoupling needs to be made. Therefore, they are potentially effective for different line characteristics, although no detailed study has been performed until now.

As a second open point, the conventional parameter tuning is cumbersome, and the region of the achievable performance is narrow. Until now, classic design methods, e.g, root locus [27] and frequency-domain analysis [28], [29], have been widely used in the design and tuning of the grid-forming power control loops. On the one hand, these methods are manual and trial-and-error due to the fact that only one parameter can be tuned at a time and the influences of different parameters can be conflicting, which renders the control tuning a daunting task. On the other hand, the achievable performance is limited, e.g., the eigenvalues cannot be placed to the positions beyond the root loci. As a result, the required stability and time-domain performance, e.g., settling time (T_s), percentage overshoot ($P.O.$), etc., may not be guaranteed. Some other design methods such as $\mathcal{H}_\infty$ synthesis have also been used, which are convenient to tune a multi-parameters system and to achieve an optimal performance [30]. Their performance depends on the deployed weighting functions which are hard to tune from time-domain specifications.

Third and finally, some basic properties have not been studied, e.g., the controllability [31]. As a controlled system, the controllability determines whether there exist suitable inputs that can transfer the states of the grid-forming power loops from any initial values to the equilibrium. The controllability is of great importance in control design especially for state-space models, which can be used to explain why a specific control structure is effective, i.e., the states can be controlled by the inputs.

Motivated by the aforementioned analysis, a full-state feedback based-power control has been proposed for grid-forming converters in [32], where only the basic idea and results have been given. In this paper, the details will be discussed from the perspectives of modeling, controllability, and design. Experimental validations with different line characteristics will also be presented. In summary, the proposed method has the following advantages and contributions.

1) The established error-based state-space model is a MIMO system considering the natural coupling between the active and reactive power loops. Therefore, the analysis and controller design are expected to have favorable robustness to mixed line characteristics (i.e., resistive, inductive, and complex) and grid strength (i.e., small and large short-circuit ratio (SCR)). It should be highlighted that this paper does not deliberately pursue the loop coupling like the conventional methods. In contrast, it fully take the nature coupling into consideration during the modeling and design.
2) The controllability Gramian is studied in detail for the first time, which provides a theoretical basis to the subsequent controller design.
3) A full-state feedback control design with only local measurements is proposed, where the eigenvalues can be placed at any position within the timescale of the power loops. A step-by-step parameters design procedure based on the predefined time-domain performance is provided.

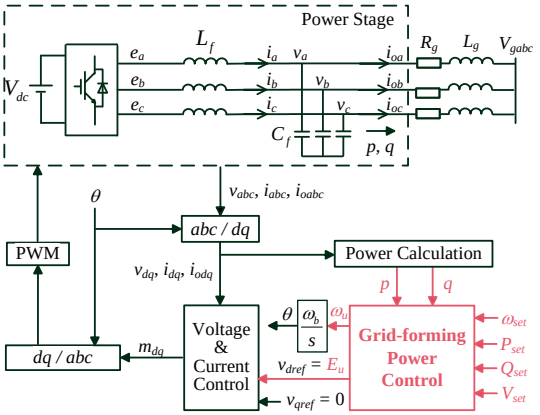

Fig. 1. General configuration of grid-forming converters with outer power control and inner cascaded control.

The remainder of paper is organized as follows. The error-based model of the grid-forming converter power loops is built in Section II. In Section III, an analysis on the controllability is carried out with the details of the full-state feedback-based power control being given in Section IV. In Section V, experimental results and system-level comparisons are shown, and finally, conclusions are given in Section VI.

II. Error-Based State-Space Modeling of Grid-Forming Converters Power Loops

Fig. 1 shows the general configuration of a grid-forming converter, where the power stage consists of a three-phase converter and an LC filter. L_f and C_f are the filter inductor and capacitor, respectively. L_g and R_g are the inductor and resistor of the line to the power grid. The grid-forming power control is responsible for providing the frequency and voltage references, i.e., ω_u and E_u, based on the calculated output active and reactive powers of the converter, i.e., p and q. Thereafter, a typical cascaded voltage and current loop is used to generate the modulation signals by regulating the capacitor voltages and inductor currents of the filter.

When considering a general line impedance ($Z_g = R_g + jX_g \neq 0$), which may be complex, the output powers p and q may couple with each other by the following equations [5]:

$$p = \frac{V^2 R_g + V V_g (X_g sin\delta - R_g cos\delta)}{R_g^2 + X_g^2} \tag{1}$$

$$q = \frac{V^2 X_g - V V_g (R_g sin\delta + X_g cos\delta)}{R_g^2 + X_g^2} \tag{2}$$

Here V and V_g are the voltage magnitudes of the capacitor and grid, respectively. Moreover, δ is the angle separation between the vectors of capacitor and grid voltages defined as

$$\dot{\delta} = \omega_b \omega - \omega_b \omega_g, \tag{3}$$

where ω and ω_g are the voltage frequencies of the capacitor and grid, and ω_b is the base value of the frequency.

The small-signal model of (1)-(3) can be derived as

$$\Delta p = k_{p\delta}\Delta\delta + k_{pV}\Delta V \tag{4}$$

$$\Delta q = k_{q\delta}\Delta\delta + k_{qV}\Delta V \tag{5}$$

$$\Delta\dot{\delta} = \omega_b\Delta\omega - \omega_b\Delta\omega_g \tag{6}$$

where

$$k_{p\delta} = \left.\frac{\partial p}{\partial \delta}\right|_{\delta_0,V_0} = \frac{V_0V_g(R_g sin\delta_0 + X_g cos\delta_0)}{R_g^2+X_g^2} \tag{7}$$

$$k_{pV} = \left.\frac{\partial p}{\partial V}\right|_{\delta_0,V_0} = \frac{2V_0R_g + V_g(X_g sin\delta_0 - R_g cos\delta_0)}{R_g^2+X_g^2} \tag{8}$$

$$k_{q\delta} = \left.\frac{\partial q}{\partial \delta}\right|_{\delta_0,V_0} = \frac{V_0V_g(X_g sin\delta_0 - R_g cos\delta_0)}{R_g^2+X_g^2} \tag{9}$$

$$k_{qV} = \left.\frac{\partial q}{\partial V}\right|_{\delta_0,V_0} = \frac{2V_0X_g - V_g(R_g sin\delta_0 + X_g cos\delta_0)}{R_g^2+X_g^2} \tag{10}$$

and the subscript "0" represent the variables corresponding to the used steady-state operation point to linearize the model.

Due to the much larger bandwidths of the cascaded loops, their quick dynamics can be neglected to obtain

$$\begin{bmatrix}\Delta\omega & \Delta V\end{bmatrix}^T = \begin{bmatrix}\Delta\omega_u & \Delta E_u\end{bmatrix}^T \tag{11}$$

where (4)-(11) consist of the regular open-loop model of the grid-forming power loops.

To share the power among multiple inverters in a potential islanded operation mode or to enable coordinated power-sharing among different generation units in a transmission grid, the steady-state droop characteristics are expected to be included in the grid-forming control. It is widely recognized that the following p-f and q-V droops should be used for an inductive line

$$\omega_u - \omega_{set} = D_p(P_{set} - p) \tag{12}$$

$$V - V_{set} = D_q(Q_{set} - q), \tag{13}$$

where D_p and D_q are the droop coefficients, the subscript "set" represents the variables corresponding to the set-point. It should be mentioned that the frequency ω_u is better than ω to be used to construct the droop characteristic due to the fact ω is not directly available in practice if not using a phase-locked loop. On the contrary, the following p-V and q-f droops should be used for a resistive line:

$$V - V_{set} = D_p(P_{set} - p) \tag{14}$$

$$\omega_u - \omega_{set} = D_q(Q_{set} - q) \tag{15}$$

As an example, in this paper, the p-f and q-V droops of (12) and (13) are used in the modeling. Nevertheless, the same method can be applied to a system with the p-V and q-f steady-state droops. In the following, it will be illustrated that the proposed control can be effective for a complex line as well. Therefore, we define the droop output $\boldsymbol{y}$ and its reference $\boldsymbol{y}_{ref}$ as

$$\boldsymbol{y} = \begin{bmatrix}y_1 & y_2\end{bmatrix}^T = \begin{bmatrix}\omega_u + D_p p & V + D_q q\end{bmatrix}^T \tag{16}$$

$$\boldsymbol{y}_{ref} = \begin{bmatrix}y_{1ref} & y_{2ref}\end{bmatrix}^T = \begin{bmatrix}\omega_{set} + D_p P_{set} & V_{set} + D_q Q_{set}\end{bmatrix}^T \tag{17}$$

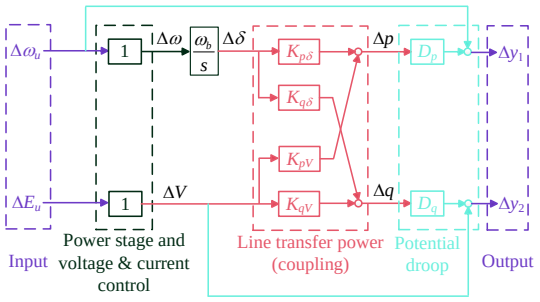

Fig. 2. Open-loop small-signal model of grid-forming power loops with droop characteristics.

Combining (4)-(11) and (16), the open-loop small-signal model of the grid-forming converter power loops with droop characteristics can be derived as

$$\Delta\dot{\delta} = \begin{bmatrix}\omega_b & 0\end{bmatrix}\begin{bmatrix}\Delta\omega_u & \Delta E_u\end{bmatrix}^T - \omega_b\Delta\omega_g \tag{18}$$

$$\Delta\boldsymbol{y} = \begin{bmatrix}D_pk_{p\delta}\\ D_qk_{q\delta}\end{bmatrix}\Delta\delta + \begin{bmatrix}1 & D_pk_{pV}\\ 0 & 1+D_qk_{qV}\end{bmatrix}\begin{bmatrix}\Delta\omega_u\\ \Delta E_u\end{bmatrix} \tag{19}$$

which is illustrated in Fig. 2. Clearly, it represents a two-input two-output system. The grid-forming control aims to find proper closed-loop controllers so that the outputs $\boldsymbol{y}$ can track the reference $\boldsymbol{y}_{ref}$ with zero steady-state errors by favorable dynamics. Therefore, in the following, we establish the error-based model and transfer the tracking problem to a regulator problem for the convenience of analysis and design.

To this end, define the error signals as

$$\Delta\boldsymbol{e} = \Delta\boldsymbol{y} - \Delta\boldsymbol{y}_{ref}, \tag{20}$$

where, for the step references, there is

$$\Delta\dot{\boldsymbol{e}} = \Delta\dot{\boldsymbol{y}}. \tag{21}$$

Placing (19) into (21) yields

$$\Delta\dot{\boldsymbol{e}} = \begin{bmatrix}D_pk_{p\delta}\\ D_qk_{q\delta}\end{bmatrix}\Delta\dot{\delta} + \begin{bmatrix}1 & D_pk_{pV}\\ 0 & 1+D_qk_{qV}\end{bmatrix}\begin{bmatrix}\Delta\dot{\omega}_u\\ \Delta\dot{E}_u\end{bmatrix} \tag{22}$$

which, with (18), is not yet a standard state-space model. Therefore, we define the following intermediate state Δz and input $\Delta\boldsymbol{u}$

$$\Delta z = \Delta\dot{\delta},\ \Delta\boldsymbol{u} = \begin{bmatrix}\Delta u_1 & \Delta u_2\end{bmatrix}^T = \begin{bmatrix}\Delta\dot{\omega}_u & \Delta\dot{E}_u\end{bmatrix}^T. \tag{23}$$

The error-based state-space model of the grid-forming converter power loops can then be stated as

$$\Delta\dot{\boldsymbol{x}} = \boldsymbol{A}\Delta\boldsymbol{x} + \boldsymbol{B}\Delta\boldsymbol{u} \tag{24}$$

and the state vector $\Delta\boldsymbol{x}$, state matrix $\boldsymbol{A}$, and control matrix $\boldsymbol{B}$ are defined as

$$\Delta\boldsymbol{x} = \begin{bmatrix}\Delta\boldsymbol{e}\\ \Delta z\end{bmatrix},\ \boldsymbol{A} = \begin{bmatrix}0 & 0 & D_pk_{p\delta}\\ 0 & 0 & D_qk_{q\delta}\\ 0 & 0 & 0\end{bmatrix},\ \boldsymbol{B} = \begin{bmatrix}1 & D_pk_{pV}\\ 0 & 1+D_qk_{qV}\\ \omega_b & 0\end{bmatrix} \tag{25}$$

Compared with the original model of (4)-(11), the model of (24) takes the droop error $\Delta\boldsymbol{e}$ and the frequency error Δz as the states. As a result, once a closed-loop controller is designed to provide a favorable (stable) dynamic performance, the steady-state droop regulation and the frequency

synchronization will be asymptotically guaranteed (in presence of step disturbances) according to the internal model principle [33]. It is worth mentioning that the built open-loop model in this section is universal, which can be used to design various closed-loop grid-forming control structures.

III. Analysis on Controllability Gramian

Before going on with the controller design, this section investigates controllability, i.e., whether the states can be controlled by the inputs. The controllability governs the existence of the studied control design problem in theory. For a given state-space model, if it is not controllable, a proper input may never be found whatever static or dynamic gains are chosen. The analysis in this section uses the following lemma.

Lemma 1 [34]. *Given the state-space model of (24), where $\boldsymbol{A}$ is an $n\times n$ matrix, the system is controllable if and only if the controllability Gramian $\boldsymbol{P_T}$ is nonsingular, where*

$$\boldsymbol{P_T} \triangleq \int_0^t e^{\boldsymbol{A}\tau}\boldsymbol{B}\boldsymbol{B}^T e^{\boldsymbol{A}^T\tau} d\tau. \tag{26}$$

It is noticed, according to (25), that

$$\boldsymbol{A}^2 = 0, \tag{27}$$

which yields that

$$e^{\boldsymbol{A}\tau} = \boldsymbol{I}+\boldsymbol{A}\tau,\ e^{\boldsymbol{A}^T\tau} = \boldsymbol{I}+\boldsymbol{A}^T\tau \tag{28}$$

Therefore, the controllability Gramian (26) is equivalent to

$$\boldsymbol{P_T} \triangleq \int_0^t (\boldsymbol{I}+\boldsymbol{A}\tau)\boldsymbol{B}\boldsymbol{B}^T(\boldsymbol{I}+\boldsymbol{A}^T\tau) d\tau, \tag{29}$$

where the final result is shown as (30) on the top of next page. To guarantee the nonsingularity of $\boldsymbol{P_T}$, its determinant should be nonzero, i.e.,

$$1/12 D_p^2\omega_b^4(k_{p\delta}+D_q k_{p\delta}k_{qV}-D_q k_{pV}k_{q\delta})^2 t^5 \neq 0 \tag{31}$$

Remark 1. *The controllability Gramian is a quantitative metric. The further its determinant is bounded away from zero the easier it is to control the system. The controllability Gramian reflects how much energy is needed to control the system and can be used to construct a so-called minimal energy control, which will, however, not be further discussed in this paper.*

Substituting (7)-(10) into (31) yields

$$F_c \triangleq \frac{D_p V_0 V_g(R_g sin\delta_0 + X_g cos\delta_0 - D_q V_g + 2V_0 D_q cos\delta_0)}{R_g^2+X_g^2} \neq 0 \tag{32}$$

Remark 2. *The condition (32) holds in usual as $D_p V_0 V_g \neq 0$ in a normal operation and $2V_0 cos\delta_0 \geq V_g$ for a small δ_0, which leads to $F_c > 0$. Even through $F_c = 0$ for some large δ_0, when the system is deviated from the equilibrium (δ_0, V_0) due to disturbances (both external disturbances and set-points changing), there is $F_c \neq 0$ and the system is controllable.*

Now consider a resistive line by setting $X_g = 0$, where F_c becomes

$$F_c = \frac{D_p V_0 V_g(R_g sin\delta_0 - D_q V_g + 2V_0 D_q cos\delta_0)}{R_g^2} \tag{33}$$

which means that although the $p-f$ and $q-V$ droops of (12) and (13) are applied to a resistive line, the system may still be controllable. That is to say, the steady-state droop characteristics can be decoupled with the line characteristics. Similarly, it can be proved that the $p-V$ and $q-f$ droops of (14) and (15) can also be applied to an inductive network. Nevertheless, these conclusions are only related to an ideal model (without physical restraints). It still prefers to use the $p-V$ and $q-f$ droops to a resistive line. Otherwise, the grid-forming converter may need to absorb large reactive power to output the required active power.

Remark 3. *The condition (32) is also effective for different (non-zero) SCRs, i.e, the system can be controllable when connected into power grids with different strengths.*

IV. Full-State Feedback Design

This section first presents how to construct the feedback loops based on the full-state feedback control. Then a step-by-step gains design based on the predefined time-domain specifications is given. It should be highlighted that the controllability check in Section III is necessary for the following design.

A. Control Law Construction

To construct the feedback laws, the following lemma is used.

Lemma 2 [31]. *Given the state-space model of (24), the close-loop poles can be placed at arbitrary locations by the following control law if and only if the system is controllable.*

$$\Delta\boldsymbol{u} = -\boldsymbol{K}\Delta\boldsymbol{x} \tag{34}$$

where $\boldsymbol{K}$ is a static gain matrix.

The studied error-based state-space model in this paper represents a system with three states and two inputs, according to **Lemma 2**, the gain matrix $\boldsymbol{K}$ can be expressed as

$$\boldsymbol{K} = \begin{bmatrix} k_{11} & k_{12} & k_{13} \\ k_{21} & k_{22} & k_{23} \end{bmatrix} \tag{35}$$

where k_{ij} is the control gain. Placing (35) and the specific forms, corresponding to the grid-forming power loops, of $\Delta\boldsymbol{u}$ (23) and $\Delta\boldsymbol{x}$ (25) into (34) yields

$$\begin{bmatrix} \Delta\dot{\omega}_u \\ \Delta\dot{E}_u \end{bmatrix} = \begin{bmatrix} k_{11} & k_{12} \\ k_{21} & k_{22} \end{bmatrix} \begin{bmatrix} -\Delta e_1 \\ -\Delta e_2 \end{bmatrix} - \begin{bmatrix} k_{13} \\ k_{23} \end{bmatrix} \Delta z \tag{36}$$

where the actual inputs provided by the grid-forming power control, combing with the definition of Δz (23), are derived as

$$\begin{bmatrix} \Delta\omega_u \\ \Delta E_u \end{bmatrix} = -\int_0^t \left(\begin{bmatrix} k_{11} & k_{12} \\ k_{21} & k_{22} \end{bmatrix} \begin{bmatrix} e_1 \\ e_2 \end{bmatrix} \right) d\tau - \begin{bmatrix} k_{13} \\ k_{23} \end{bmatrix} \Delta\delta \tag{37}$$

Until now, the design of the close-loop structure for the grid-forming power loops assumes that all the necessary signals are measurable. Nevertheless, $\Delta\delta$ may not be locally available due to the fact that $\Delta\omega_g$ is a remote disturbance signal. A state observer can be used to solve this problem, which will not be discussed further to focusing this paper on the full-state feedback. Instead, the actual $\Delta\delta$ can be simply estimated using (4) and (5) as

$$\Delta\hat{\delta} = k_p\Delta p - k_q\Delta q \tag{38}$$

$$\boldsymbol{P_T} = \begin{bmatrix} 1/3\omega_b^2 D_p^2 k_{p\delta}^2 t^3 + \omega_b D_p k_{p\delta} t^2 + (1+D_p^2 k_{pV}^2)t & 1/3\omega_b^2 D_p D_q k_{p\delta} k_{q\delta} t^3 + 1/2\omega_b D_q k_{q\delta} t^2 + D_p k_{pV}(1+D_q k_{qV}^2)t & 1/2\omega_b^2 D_p k_{p\delta} t^2 + \omega_b t \\ 1/3\omega_b^2 D_p D_q k_{p\delta} k_{q\delta} t^3 + 1/2\omega_b D_q k_{q\delta} t^2 + D_p k_{pV}(1+D_q k_{qV}^2)t & 1/3\omega_b^2 D_q^2 k_{q\delta}^2 t^3 + (1+D_q k_{qV})^2 t & 1/2\omega_b^2 D_q k_{q\delta} t^2 \\ 1/2\omega_b^2 D_p k_{p\delta} t^2 + \omega_b t & 1/2\omega_b^2 D_q k_{q\delta} t^2 & \omega_b^2 t \end{bmatrix} \tag{30}$$

where

$$k_p = \frac{K_{qV}}{K_{p\delta}K_{qV} - K_{pV}K_{q\delta}},\ k_q = \frac{K_{pV}}{K_{p\delta}K_{qV} - K_{pV}K_{q\delta}} \tag{39}$$

Finally, the complete close-loop small-signal model of the proposed full-state feedback-based grid-forming converter can be shown as Fig. 3. Therefore, the representative block diagram of the proposed power control is shown in Fig. 4. It is worth mentioning that (38) is only used to estimate $\Delta\delta$, which is not a part of the full-state feedback control law.

Remark 4. *The proposed general control architecture allows to reproduce all existing partial-state feedback ones as well as any other linear time-invariant feedback connection between the considered signals. For example, by setting* $k_{12} = k_{21} = k_{13} = k_{23} = 0$*, the proposed MIMO full-state feedback-based grid-forming structure becomes the traditional VSG assuming a (p, f) and (q, V) decoupling, i.e., the VSG control is a special case of the proposed structure with simplified SISO loops and partial-state feedback. However, these four parameters* k_{12}*,* k_{21}*,* k_{13}*,* k_{23} *couple the active and reactive power loops. As a result, the proposed MIMO structure has good robustness to line impedance characteristics.*

B. Parameters Design

By applying the full-state feedback control law of (34), the closed-loop state-space model of (24) is derived as

$$\Delta\dot{\boldsymbol{x}} = (\boldsymbol{A} - \boldsymbol{B}\boldsymbol{K})\Delta\boldsymbol{x} \tag{40}$$

where its characteristic equation is

$$|\lambda\boldsymbol{I} - \boldsymbol{A} + \boldsymbol{B}\boldsymbol{K}| = 0 \tag{41}$$

The characteristic equation (41) has three eigenvalues, which can be placed at arbitrary locations according to **Lemma 2**. As a reasonable choice, we choose a pair of complex eigenvalue as the dominant ones and a real eigenvalue, which is far away from the dominant eigenvalues. Therefore, the characteristic equation should has the following form

$$(\lambda + a)(\lambda^2 + 2\xi\omega_n\lambda + \omega_n^2) = 0 \tag{42}$$

where $-a$ is a chosen real eigenvalue, ξ and ω_n are the damping ratio and natural frequency of the chosen complex eigenvalues. Thereafter, the gain matrix $\boldsymbol{K}$ can be solved by

$$|\lambda\boldsymbol{I} - \boldsymbol{A} + \boldsymbol{B}\boldsymbol{K}| \equiv (\lambda + a)(\lambda^2 + 2\xi\omega_n\lambda + \omega_n^2) \tag{43}$$

which always has solutions due to **Lemma 2**. Placing (25) and (35) into (43) yields

$$k_{11} + k_{22} + k_{13}\omega_b + k_{21}D_p k_{pV} + k_{22}D_q k_{qV} = a + 2\xi\omega_n \tag{44}$$

$$\begin{aligned}&[k_{11}k_{22} - k_{12}k_{21} - (k_{12}k_{23} - k_{13}k_{22})\omega_b](1 + D_q k_{qV}) \\ &+ k_{11}\omega_b D_p k_{p\delta} + k_{12}\omega_b D_q k_{q\delta} - (k_{11}k_{23} - k_{13}k_{21})\omega_b D_p k_{pV} \\ &= 2a\xi\omega_n + \omega_n^2\end{aligned} \tag{45}$$

$$(k_{11}k_{22} - k_{12}k_{21})\omega_b D_p(k_{p\delta} + D_q k_{p\delta} k_{qV} - D_q k_{pV} k_{q\delta}) = a\omega_n^2 \tag{46}$$

Moreover, time-domain performance is one of the commonly used indices in practice. For a dominant second-order system, i.e., assuming $-a$ is far in the left half plane, the time-domain performance has direct relationship with ξ and ω_n [31], e.g., by taking *P.O.* and T_s as examples in this paper,

$$P.O. = e^{-(\xi/\sqrt{1-\xi^2})} \times 100\% \tag{47}$$

$$T_s = \frac{4}{\xi\omega_n} \tag{48}$$

which implies that the dominant complex eigenvalues can be calculated by the predefined time domain performance.

In summary, (44)-(48) represent the relationships between the time-domain performance and the controller gains. For a MIMO system, the solutions are usually not unique, where, we can use the degrees of freedom to provide good robustness [31]. Such task can be carried out automatically through the command *place* of Matlab.

According to the aforementioned discussion, a step-by-step parameter design procedure for the proposed full-state feedback-based grid-forming control can be summarized as follows.

- step 1: Preparation. Before designing the parameters, it should know the predefined time-domain performance as defined by the expected locations of the eigenvalues (ξ, ω_n, and a) according to (47) and (48).
- step 2: Linearization. Choosing the steady-state operation point (δ_0, V_0) to get the linearized system parameters $K_{p\delta}$, K_{pV}, $K_{q\delta}$, K_{qV}, $\boldsymbol{A}$, and $\boldsymbol{B}$ according to (7)-(10) and (25).
- step 3: Controllability checking. The judgment is based on (32).
- step 4: Parameters calculation. k_p and k_q can be calculated according to (39). $\boldsymbol{K}$ can be solved according to (43).

Remark 5. *The proposed method is model-based, which relies on the parameters of the system. It does not narrow the application as the traditional popular methods of root locus analysis and frequency analysis rely on the same requirement. Moreover, as the proposed method can arbitrarily place the eigenvalues, a good stability margin can be guaranteed to improve the robustness on parameter variations. Even when some parameters are completely unknown, the proposed structure can potentially have better dynamics than the widely accepted VSG control which is special case (referring to* ***Remark 4****).*

Remark 6. ***Lemma 2*** *has provided an exact condition to arbitrarily placed the eigenvalues of the system. Therefore, any additional loops to improve the stability are unnecessary. However, they may improve the transient performance.* ***Lemma 2*** *guarantees the superiority of the proposed method compared to other grid-forming controls.*

Remark 7. *Although there is* ***Remark 6****, it is only related to the eigenvalues (poles) of the grid-forming power loops. Other issues may still need further study, e.g., issues related to the zeros, systems beyond Fig. 1, coupled power loops and cascaded loops, etc.*

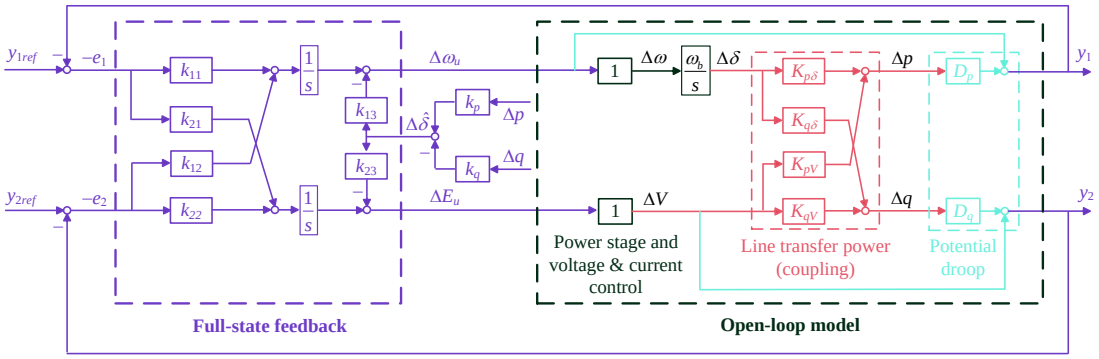

Fig. 3. Close-loop small-signal model of proposed full-state feedback-based grid-forming converter.

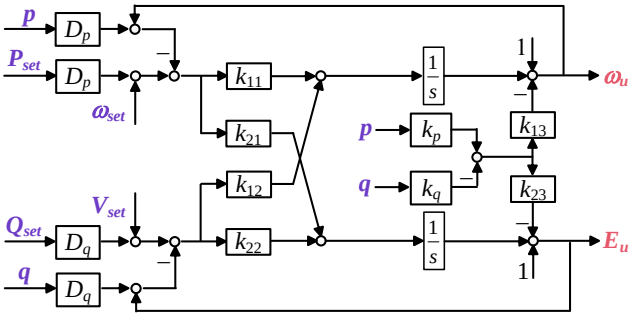

Fig. 4. Representative block diagram of proposed power control strategy. (The purple signals are inputs and the red are outputs of the control.)

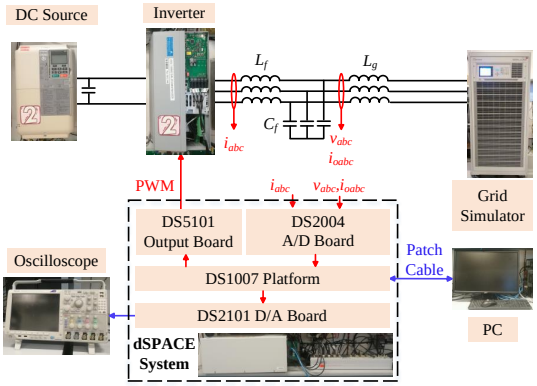

Fig. 5. Experimental configuration of grid-forming converter.

For a controllable system, other methods rather than the used pole placement method may also be applied, e.g., the linear quadratic regulator (LRQ), to achieve an optimal design, which could be a future work.

V. Experimental Validation and System-Level Comparison

A. Experimental Validation

To verify the proposed full-state feedback control structure and parameter design for power loops of the grid-forming converter, this section will present some experimental results. The configuration of the setup is shown in Fig. 5, where the power stage consists of a Danfoss drives system, an LCL filter and a Chroma 61845 grid simulator. The control is implemented by the DS1007 dSPACE system. Meanwhile, the DS2004 A/D board and DS2101 D/A board are used to collect the measurements and generate the output, respectively. The used key parameters are given in Table I if there is no specific illustration.

1) Test on Different Predefined Time-domain Performance: In this section, the dynamics of the proposed controller and parameter design method is tested with different predefined time-domain performance (i.e., *P.O.* and T_s). The step-by-step parameter design is exerted as follows.

- step 1: Preparation.
  Four different studied cases are used as shown in Table II. The locations of the dominant complex eigenvalues are also presented in Fig. 6. As mentioned above, it is usually favorable to have a pair of dominant complex eigenvalues. A general principle is that the third eigenvalue should be at least 5 times far away from the imaginary axis compared to the complex eigenvalues [31]. Meanwhile, although the third eigenvalue can be arbitrarily far theoretically according to the full-state feedback, it is impossible in practice. Too far away of the third eigenvalue will, on the one hand, lead to coupling with the dynamics of the inner loops, which makes the assumption of loops decoupling fail, and on the other hand, require very large gain $\boldsymbol{K}$, which deteriorates the

TABLE I
Parameters of Experimental Setups

Symbol	Description	Value
f_n	Nominal frequency	100π rad/s
S_n	Nominal power	5 kW
V_n	Nominal line-to-line RMS voltage	200 V
f_{sw}	Switching frequency	10 kHz
ω_g	Grid frequency	100π rad/s (1 p.u.)
V_g	Line-to-line RMS grid voltage	200 V (1 p.u.)
L_g	Line inductor	2.5 mH (0.0982 p.u.)
C_f	Filter capacitor	15 μF (0.0377 p.u.)
L_f	Filter inductor	1.5 mH (0.0589 p.u.)
D_p	Droop coefficient of P-f regulation	0.01 p.u.
D_q	Droop coefficient of Q-V regulation	0.05 p.u.
ω_{set}	Frequency reference	1 p.u.
P_{set}	Active power reference	0.5 p.u.
Q_{set}	Reactive power reference	0 p.u.
V_{set}	Voltage magnitude reference	1 p.u.

TABLE II
STUDIED CASES TO PLACE EIGENVALUES

Cases	Damping Ratio ξ	Settling Time T_s	Third eigenvalue a
1	0.4	1 s	-20
2	0.4	2 s	-20
3	0.707	1 s	-20
4	0.707	2 s	-20

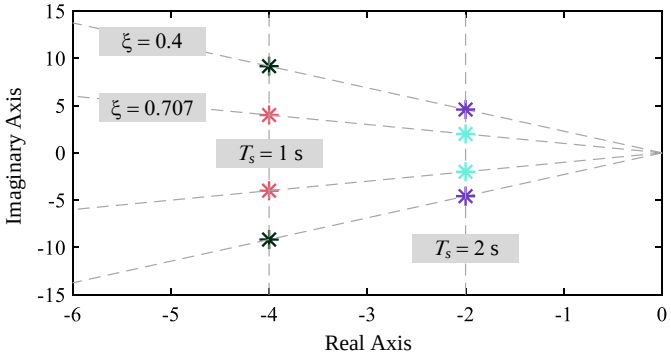

Fig. 6. Chosen dominant complex eigenvalues.

robustness of the system, i.e., a small disturbance or model inaccuracy will be enlarged by the large $\boldsymbol{K}$ to lead to instability of the system.

- step 2: Linearization.
  The steady-state operation point calculated based on Table I is (δ_0, V_0) = (0.0491, 0.9996). Thereafter, the linearized system parameters can be derived as follows.

$$(K_{p\delta}, K_{pV}, K_{q\delta}, K_{qV}) = (10.1695, 0.5002, 0.5, 10.1899) \tag{49}$$

$$\boldsymbol{A} = \begin{bmatrix} 0 & 0 & 0.1017 \\ 0 & 0 & 0.025 \\ 0 & 0 & 0 \end{bmatrix}, \ \boldsymbol{B} = \begin{bmatrix} 1 & 0.005 \\ 0 & 1.5095 \\ 314.1593 & 0 \end{bmatrix} \tag{50}$$

- step 3: Controllability checking.
  With the calculated (δ_0, V_0), there is $F_c = 0.1534 > 0$, which implies that the system is completely state controllable.
- step 4: Parameters calculation.
  The calculated control gains of different cases are listed in Table III.

Fig. 7 presents the experimental comparisons of the studied cases when P_{set} steps from 0.5 p.u. to 1 p.u.. As shown, when choosing a large damping ratio ($\xi = 0.707$ in Case 3 and Case 4), the dynamics have smaller *P.O.* than those with a small damping ratio ($\xi = 0.4$ in Case 1 and Case 2). Meanwhile, when choosing a small settling time ($T_s = 1$s in Case 1 and Case 3), the systems can reach the steady-state quicker than those with a large settle time ($T_s = 2$s in Case 2 and Case 4). Fig. 7 proves that the proposed full-state feedback control structure and parameter design method are effective to regulate time-domain performance of the power loops of the grid-forming converter.

2) Test on Complex Line: In this section, the dynamics of the proposed controller and parameter design method is tested with a complex (Case 5) line, where Case 3 with a inductive line is chosen as a base case for comparison. Therefore, the time-domain performance is set the same as Case 3 and the tested parameters of the line are listed in Table IV. The controller parameters of Case 5 based on the step-by-step design procedure are also listed in Table III.

Fig. 8 shows the experimental waveform. As observed, the dynamics is smooth and in accordance with the predefined time-domain performance, which proves the effectiveness of the proposed method to a complex line.

It should be mentioned that, for a resistive line, the proposed method is completely effective by just using the $p-V$ and $q-f$ droops instead, which will not be presented here.

3) Test on Different Grid Strengths: In this section, the dynamics of the proposed controller and parameter design method is tested with weak (Case 6) and very weak (Case 7) grids, respectively, where Case 3 (strong grid) is still chosen as a base case for comparison. The tested parameters of the SCR are listed in Table V. The controller parameters of Case 6 and 7 based on the step-by-step design procedure are listed in Table III, and the experimental comparisons are presented in Fig. 9. As shown, the proposed method has good robustness to the grid strengths.

It is worth mentioning that, the designed results of Table III are based on the nameplate values, which may deviate from the actual ones. For example, the actual value of an 1 mH inductor (without power) is about 0.9 mH according to the measurement in the lab, which implies a 10% error. Meanwhile, the equivalent resistance is neglected as well. Therefore, the presented waveform also verifies that the proposed method has a certain ability against variations of the parameter.

B. System-Level Comparison

To further show the superiority of the proposed method, this section tests the system-level performance using the IEEE 14-Bus Test System (as shown in Fig. 10(a)) in Matlab/Simulink, where G2 is replaced by a VSC with the same parameters in p.u. as Table I. The parameters of the IEEE 14-Bus Test System can be found in [35].

To design the controller parameters, the IEEE 14-Bus Test System is equivalent to a infinite bus system as shown in Fig. 10(b). The accurate equivalent impedance Z_{eq} can be obtained through network reduction techniques in [36]. Nevertheless, in this paper, it is simply supposed that Z_{eq} equals to the self impedance of Bus 2, i.e., $Z_{eq} = 0.006 + j0.02$ p.u. Apparently, this is a very inaccurate approximation. Therefore, the results can show the robustness of the methods against the model inaccuracy. It should be mentioned that Fig. 10(b) is only used for the parameter design and all the following tests are carried out using the detailed model of Fig. 10(a).

The cases in Table VI are studied. As a comparison, a traditional VSG control with VI in [23], which is designed based on loop decoupling, is tested as well.

In Case 8, Z_l is pure inductive so that, for Z_g, there is $X_g/R_g = 10$. Therefore, a VI is not necessary in the VSG.

TABLE III
DESIGNED PARAMETERS OF THE CORRESPONDING CASES

Parameters	Case 1	Case 2	Case 3	Case 4	Case 5	Case 6	Case 7
k_p	0.0986	0.0986	0.0986	0.0986	0.0736	0.4177	0.5671
k_q	0.0048	0.0048	0.0048	0.0048	0.0788	0.081	0.1413
k_{11}	3.1326	0.7832	1.0027	0.2507	1.1707	4.1083	5.4297
k_{12}	-0.0104	-0.0026	-0.0033	-0.0008	-0.0614	-0.0182	-0.0247
k_{13}	0.0155	0.0102	0.0223	0.0119	0.0217	0.0124	0.0082
k_{21}	0.037	0.0422	0.0417	0.0434	0.7435	0.0624	0.0603
k_{22}	13.2493	13.2493	13.2493	13.2493	15.0674	17.7106	18.1712
k_{23}	0.0168	0.0168	0.0167	0.0168	-0.2254	0.0222	0.0228

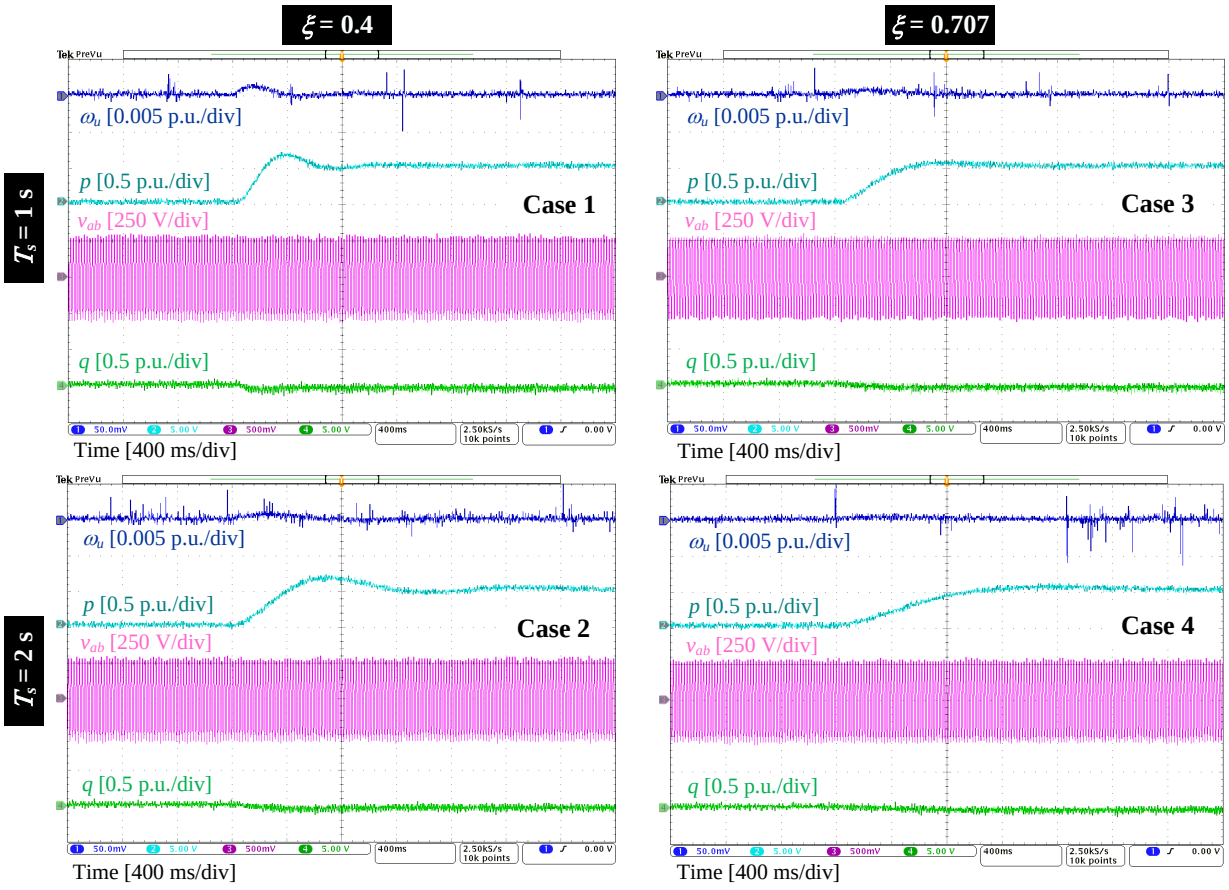

Fig. 7. Experimental comparisons with different predefined time-domain performance.

TABLE IV
STUDIED CASES OF DIFFERENT LINE CHARACTERISTICS

Cases	Line Impedance Z_g	Ratio X_g/R_g
3	$j0.0982$ p.u.	$+\infty$
5	$0.075+j0.0785$ p.u.	1.0472

TABLE V
STUDIED CASES WITH DIFFERENT SCRS

Cases	Line Impedance Z_g	SCR
3	$j0.0982$ p.u.	10.1859
6	$j0.3927$ p.u.	2.5465
7	$j0.5105$ p.u.	1.9588

In Case 9, a small resistor is added in Z_l making $X_g/R_g = 6$. In this context, R_g cannot be directly neglected. Therefore, for the VSG control, a VI of $j0.04$ p.u. is added so that the equivalent ratio of X/R is increased to 10. Then the parameters can be designed again by neglecting the resistor.

In Case 10, the resistor is enlarged further so that X_g/R_g is only 3. For the conventional VSG control, a larger VI of $j0.14$ p.u. should added so that the equivalent ratio of X/R is increased to 10 again in order to design the parameters by

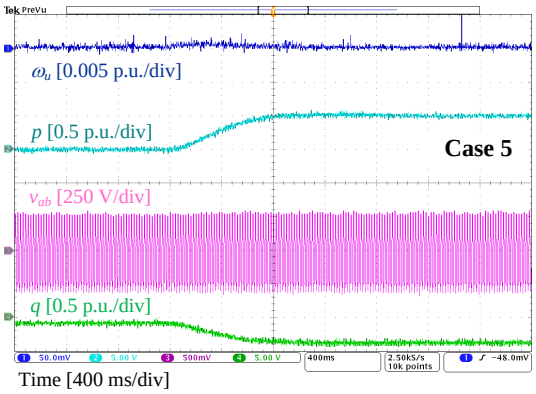

Fig. 8. Experimental results with complex line.

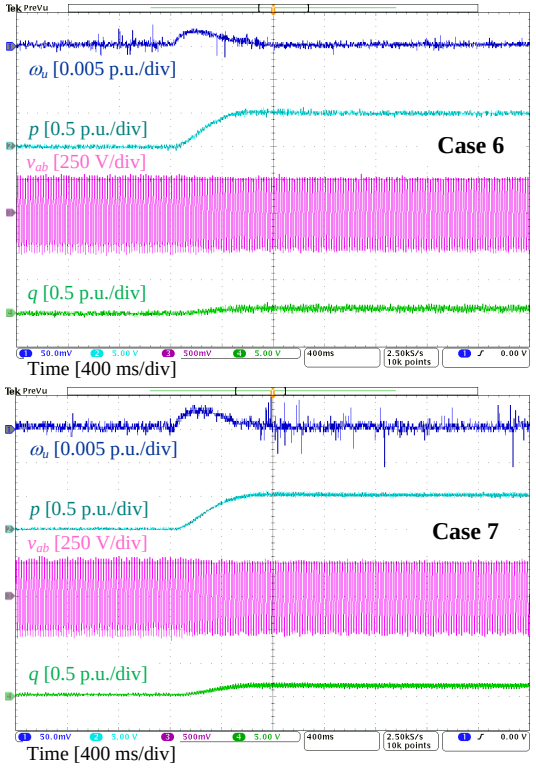

Fig. 9. Experimental comparisons with different SCRs.

TABLE VI
STUDIED CASES OF DIFFERENT Z_l IN IEEE 9-BUS TEST SYSTEM

Cases	Z_l	Z_g	X_g/R_g
8	j0.04 p.u.	0.006+j0.06 p.u.	10
9	0.004+j0.04 p.u.	0.01+j0.06 p.u.	6
10	0.014+j0.04	0.02+j0.06 p.u.	3

considering the decoupling between the active and reactive power loops.

For all of the above three cases, the parameters of the proposed method are designed so that $\xi = 0.707$ and $T_s = 1$ s just like Case 3. In terms of the VSG control, in [23], the active power loop is a 2nd-order system, where K_{ip} (the key parameter of active power loop in [23]) is chosen so that $\xi = 0.707$ as well for a fair comparison. Meanwhile, the

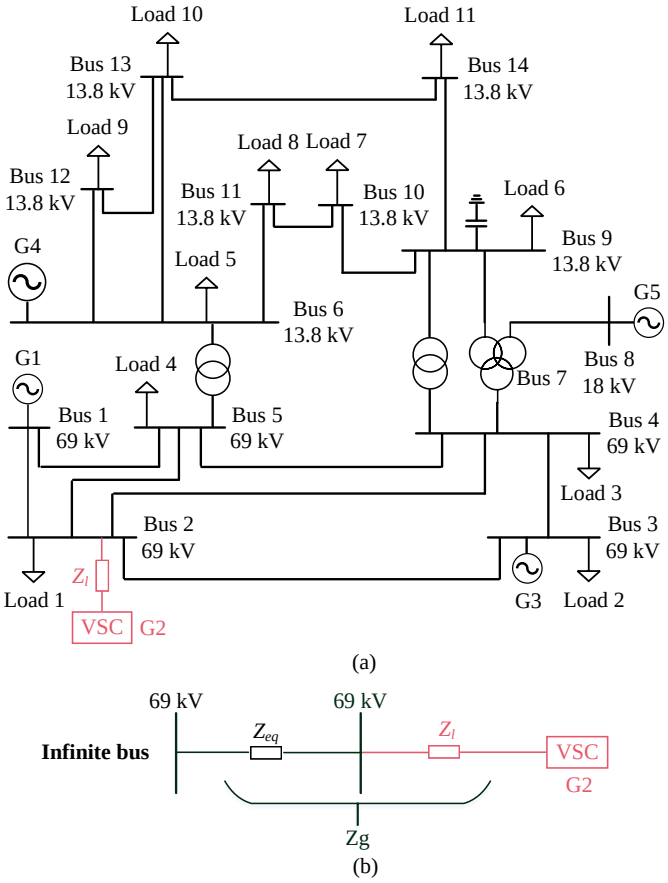

Fig. 10. IEEE 14-Bus Test System. (a) Detailed model. (b) Supposed model for parameter design.

TABLE VII
DESIGNED PARAMETERS OF THE CORRESPONDING CASES FOR SYSTEM-LEVEL TEST

Parameters (p.u.)		Case 8	Case 9	Case 10
VSG [23]	K_{ip}	1.2484	0.7496	0.373
	K_{iq}	0.548	0.911	1.8026
Proposed	k_p	0.0598	0.0597	0.0592
	k_q	0.0078	0.0118	0.0218
	k_{11}	0.5105	0.514	0.5329
	k_{12}	-0.006	-0.0091	-0.0168
	k_{13}	0.0199	0.0199	0.0198
	k_{21}	0.1259	0.1906	0.3509
	k_{22}	10.9581	11.0438	11.4244
	k_{23}	-0.0307	-0.0597	-0.1274

reactive power loop is a 1st-order system, where K_{iq} (the key parameter of reactive power loop in [23]) is chosen so that $a = -20$ as well. The designed parameters are summarized in Table VII.

The following disturbances are applied:

1) $t = 10$ s, P_{set} of the VSC increases from 0.5 p.u. to 0.8 p.u.;
2) $t = 14$ s, the output of G3 increases 0.2 p.u.;
3) $t = 18$ s, a load step of 26+j5 MVA (10% of the total

load) is added to Load 1.

Fig. 11 and Fig. 12 compare their support performance to the load bus (taking Load 1, Load 3, and Load 5 as examples) frequencies and voltages, respectively. As observed, in all three cases, both methods can keep the stable operation of the system, which shows their effectiveness. However, the load bus frequencies and voltages are with smaller oscillations with the proposed methods, especially against the disturbances from the VSI itself and load. Meanwhile, it is obviously shown that the rates of change of frequency (RoCoFs) with the proposed method are much smaller than with the conventional VSG with VI control.

To further show the superiority of the proposed method, Fig. 13 compares the output powers of the VSI with different control methods in the studied cases. As observed, when P_{set} increases at $t = 10$ s, the VSI with the proposed control can smoothly change its output power while the VSG will have obvious oscillation. When G3 output more power at $t = 14$ s, the VSI with the proposed control can actively decrease more power than the VSG to keep the power balance to obtain a more stable system. It is worth mentioning that such a larger power decrease implies a better ability responding to disturbances and it does not mean a larger oscillation. Similarly, when the load increases at $t = 18$ s, the VSI with the proposed control can provide more transient power to support the system. In Fig. 13, the dynamics of the VSG with double inertia are also presented. It is noticed that a larger inertia makes the VSG more oscillatory (from the dynamics when P_{set} increases). Therefore, the VSG cannot obtain equally favorable closed-loop dynamics as the proposed method by changing its inertia.

VI. Conclusion

This paper investigates the grid-forming converter power loops from the perspective of MIMO systems. An error-based regulator model is built by considering the potential coupling of power loops and steady-state droops. Thereafter, the controllability is studied, which reveals the ability of the inputs to control the states. A full-state feedback control strucuture and a step-by-step pole placement-based parameter design method are proposed, which can arbitrarily locate the eigenvalues of the system. The experimental results verify that the work of this paper is effective to cope with different time-domain performance, line characteristics, and grid strengths. The system-level effectiveness of the proposed method is also verified using the IEEE 14-Bus Test System, which shows a better performance than the conventional VSG with VI control.

References

[1] R. Rosso, X. Wang, M. Liserre, X. Lu, and S. Engelken, "Grid-forming converters: Control approaches, grid-synchronization, and future trends—a review," *IEEE Open J. Ind. Appl.*, vol. 2, pp. 93–109, Apr. 2021.

[2] H. Deng, J. Fang, Y. Qi, Y. Tang, and V. Debusschere, "A generic voltage control for grid-forming converters with improved power loop dynamics," *IEEE Trans. Ind. Electron.*, vol. 70, no. 4, pp. 3933–3943, Apr. 2022.

[3] Z. Li, Z. Cheng, S. Li, J. Si, J. Gao, W. Dong, and H. S. Das, "Virtual synchronous generator and SMC-based cascaded control for voltage-source grid-supporting inverters," *IEEE J. Emerg. Sel. Top. Power Electron.*, vol. 10, no. 3, pp. 2722–2736, Jun. 2022.

[4] J. Song, M. Cheah-Mane, E. Prieto-Araujo, and O. Gomis-Bellmunt, "Short-circuit analysis of AC distribution systems dominated by voltage source converters considering converter limitations," *IEEE Trans. Smart Grid*, vol. 13, no. 5, pp. 3867–3878, Sep. 2022.

[5] N. Mohammed and M. Ciobotaru, "Adaptive power control strategy for smart droop-based grid-connected inverters," *IEEE Trans. Smart Grid*, vol. 13, no. 3, pp. 2075–2085, May 2022.

[6] M. Chen, D. Zhou, C. Wu, and F. Blaabjerg, "Characteristics of parallel inverters applying virtual synchronous generator control," *IEEE Trans. Smart Grid*, vol. 12, no. 6, pp. 4690–4701, Nov. 2021.

[7] M. Chen, D. Zhou, and F. Blaabjerg, "Enhanced transient angle stability control of grid-forming converter based on virtual synchronous generator," *IEEE Trans. Ind. Electron.*, vol. 69, no. 9, pp. 9133–9144, Sep. 2022.

[8] M. Ali, J. Li, L. Callegaro, H. I. Nurdin, and J. E. Fletcher, "Regulation of active and reactive power of a virtual oscillator controlled inverter," *IET Gener. Transm. Distrib.*, vol. 14, no. 1, pp. 62–69, Jan. 2020.

[9] A. Tayyebi, D. Gross, A. Anta, F. Kupzog, and F. Dörfler, "Frequency stability of synchronous machines and grid-forming power converters," *IEEE J. Emerg. Sel. Top. Power Electron.*, vol. 8, no. 2, pp. 1004–1018, Jun. 2020.

[10] X. Quan, A. Q. Huang, and H. Yu, "A novel order reduced synchronous power control for grid-forming inverters," *IEEE Trans. Ind. Electron.*, vol. 67, no. 12, pp. 10 989–10 995, Dec. 2020.

[11] H. Zhang, W. Xiang, W. Lin, and J. Wen, "Grid forming converters in renewable energy sources dominated power grid: Control strategy, stability, application, and challenges," *J. Mod. Power Syst. Clean Energy*, vol. 9, no. 6, pp. 1239–1256, Nov. 2021.

[12] A. Tayyebi, A. Anta, and F. Dörfler, "Grid-forming hybrid angle control and almost global stability of the DC-AC power converter," *IEEE Trans. Autom. Control*, 2022.

[13] J. Yang, C. K. Tse, M. Huang, and X. Fu, "Homoclinic bifurcation of a grid-forming voltage source converter," *IEEE Trans. Power Electron.*, vol. 36, no. 11, pp. 13 176–13 187, Nov. 2021.

[14] X. Fu, J. Sun, M. Huang, Z. Tian, H. Yan, H. H.-C. Iu, P. Hu, and X. Zha, "Large-signal stability of grid-forming and grid-following controls in voltage source converter: A comparative study," *IEEE Trans. Power Electron.*, vol. 36, no. 7, pp. 7832–7840, Jul. 2021.

[15] S. Eberlein and K. Rudion, "Impact of inner control loops on small-signal stability and model-order reduction of grid-forming converters," *IEEE Trans. Smart Grid*, pp. 1–1, Nov. 2022.

[16] C. Yang, L. Huang, H. Xin, and P. Ju, "Placing grid-forming converters to enhance small signal stability of PLL-integrated power systems," *IEEE Trans. Power Syst.*, vol. 36, no. 4, pp. 3563–3573, Jul. 2021.

[17] R. Musca, A. Vasile, and G. Zizzo, "Grid-forming converters. a critical review of pilot projects and demonstrators," *Renew. Sustain. Energy Rev.*, vol. 165, pp. 1–13, Sep. 2022.

[18] F. Zhao, X. Wang, and T. Zhu, "Low-frequency passivity-based analysis and damping of power-synchronization controlled grid-forming inverter," *IEEE J. Emerg. Sel. Top. Power Electron.*, vol. 11, no. 2, pp. 1542–1554, Apr. 2022.

[19] Z. Wang, Y. Chen, X. Li, Y. Xu, C. Luo, Q. Li, and Y. He, "Active power oscillation suppression based on decentralized transient damping control for parallel virtual synchronous generators," *IEEE Trans. Smart Grid*, pp. 1–1, 2022.

[20] M. Chen, D. Zhou, A. Tayyebi, E. Prieto-Araujo, F. Dörfler, and F. Blaabjerg, "Generalized multivariable grid-forming control design for power converters," *IEEE Trans. Smart Grid*, vol. 13, no. 4, pp. 2873–2885, Jul. 2022.

[21] Q.-C. Zhong, "Robust droop controller for accurate proportional load sharing among inverters operated in parallel," *IEEE Trans. Ind. Electron.*, vol. 60, no. 4, pp. 1281–1290, Apr. 2013.

[22] F. Deng, Y. Li, X. Li, W. Yao, X. Zhang, and P. Mattavelli, "A decentralized impedance reshaping strategy for balanced, unbalanced and harmonic power sharing in islanded resistive microgrids," *IEEE Trans. Sustain. Energy*, vol. 13, no. 2, pp. 743–754, Apr. 2022.

[23] H. Wu, X. Ruan, D. Yang, X. Chen, W. Zhao, Z. Lv, and Q.-C. Zhong, "Small-signal modeling and parameters design for virtual synchronous generators," *IEEE Trans. Ind. Electron.*, vol. 63, no. 7, pp. 4292–4303, Jul. 2016.

[24] J. Liu, Y. Miura, H. Bevrani, and T. Ise, "A unified modeling method of virtual synchronous generator for multi-operation-mode analyses,"

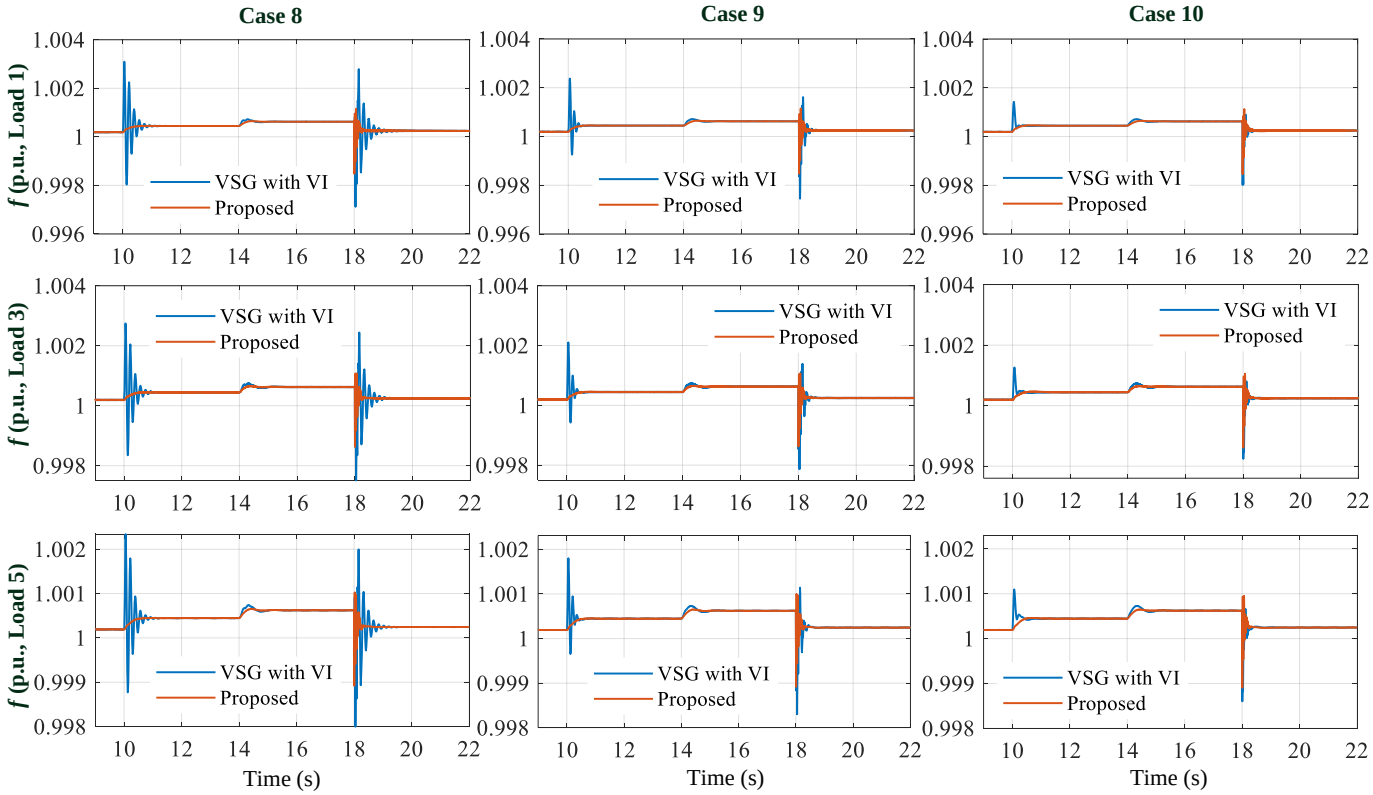

Fig. 11. System-level comparisons of load bus frequencies with different control methods.

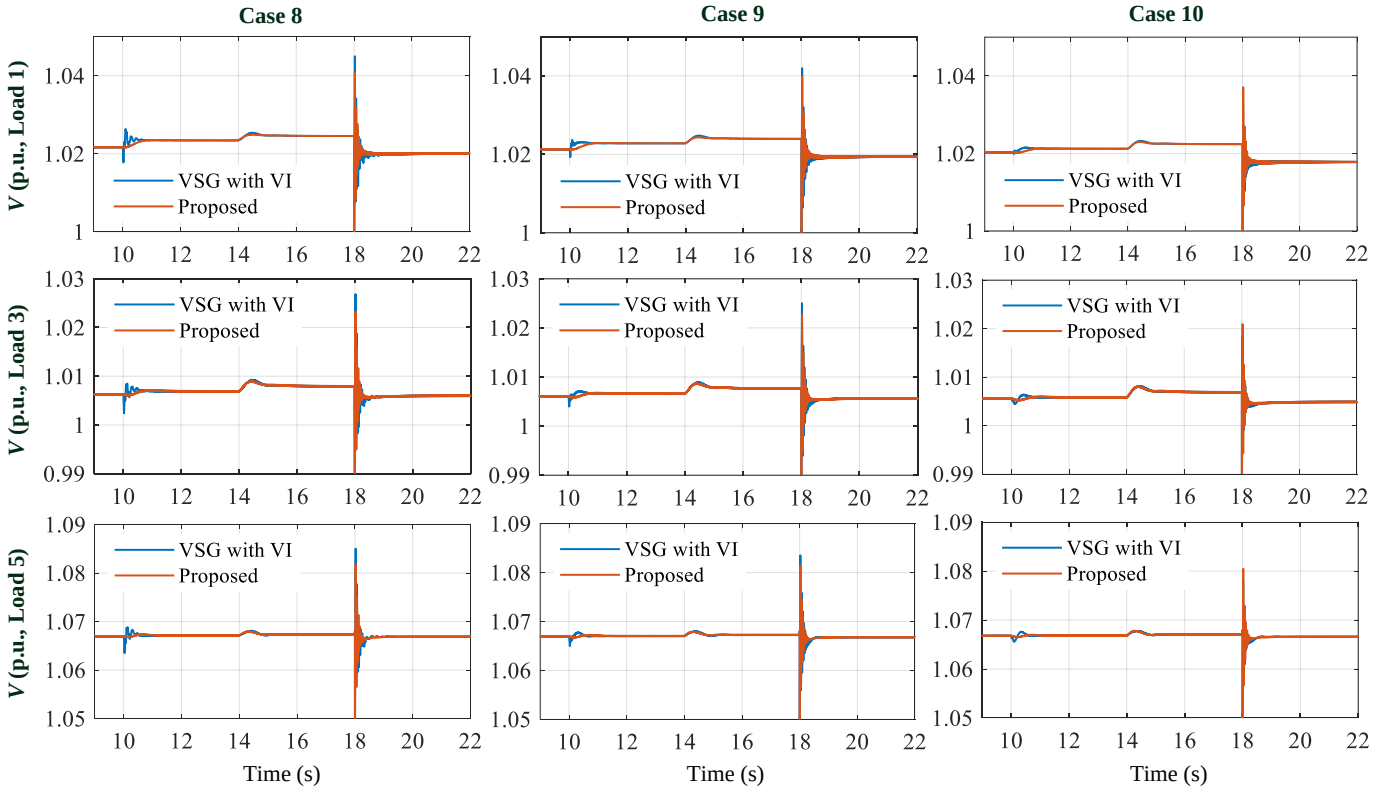

Fig. 12. System-level comparisons of load bus voltages with different control methods.

IEEE J. Emerg. Sel. Top. Power Electron., vol. 9, no. 2, pp. 2394–2409, Apr. 2021.

[25] M. Ahmed, L. Meegahapola, A. Vahidnia, and M. Datta, "Adaptive virtual impedance controller for parallel and radial microgrids with varying X/R ratios," *IEEE Trans. Sustain. Energy*, vol. 13, no. 2, pp. 830–843, Apr. 2022.

[26] A. Rafiee, Y. Batmani, H. Bevrani, and T. Kato, "Robust MIMO controller design for VSC-based microgrids: Sequential loop closing

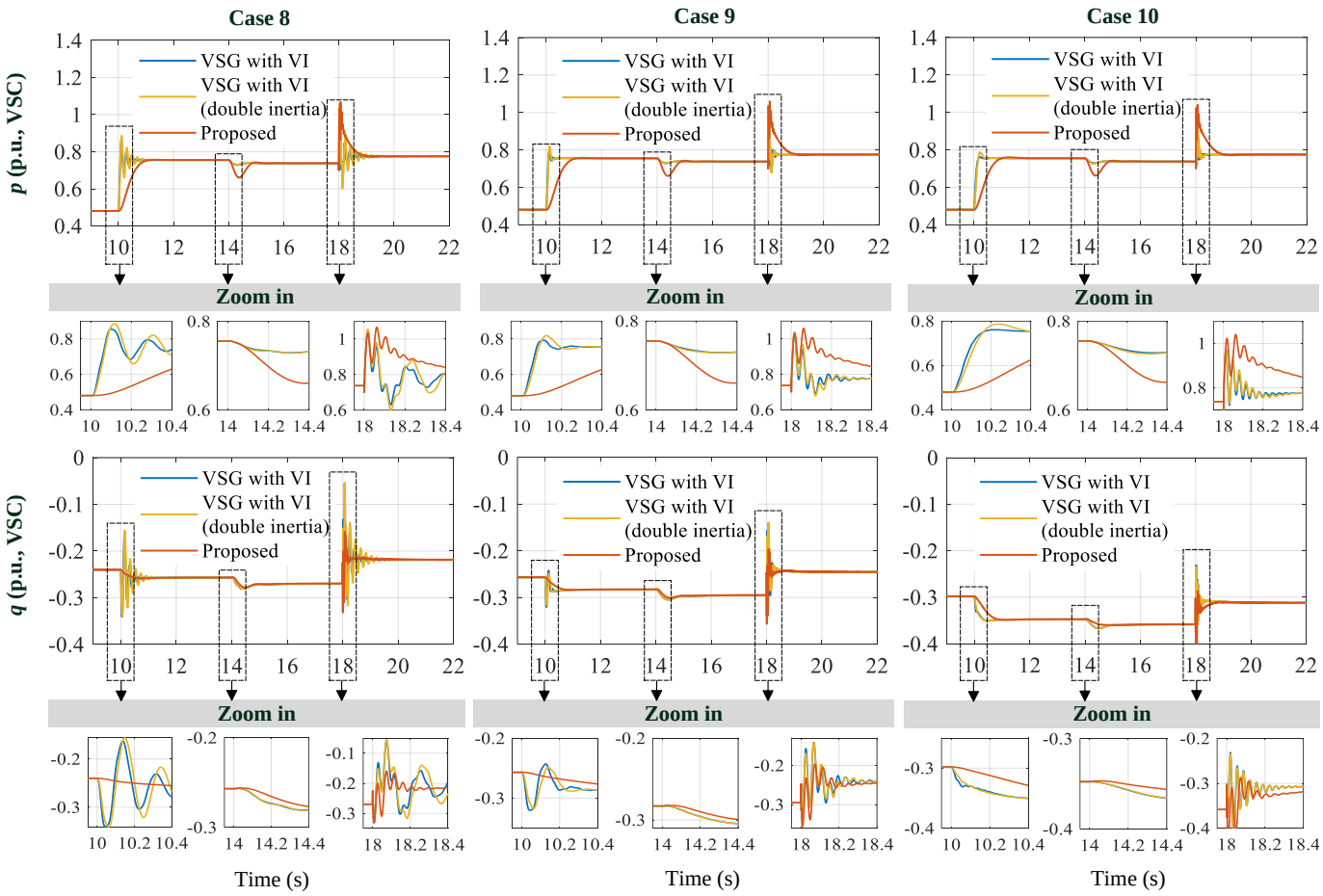

Fig. 13. System-level comparisons of output powers of VSI with different control methods.

concept and quantitative feedback theory," *IEEE Trans. Smart Grid*, vol. 13, no. 1, pp. 129–138, Jan. 2022.

[27] M. Chen, D. Zhou, and F. Blaabjerg, "Active power oscillation damping based on acceleration control in paralleled virtual synchronous generators system," *IEEE Trans. Power Electron.*, vol. 36, no. 8, pp. 9501–9510, Aug. 2021.

[28] J. Chen and T. O'Donnell, "Parameter constraints for virtual synchronous generator considering stability," *IEEE Trans. Power Syst.*, vol. 34, no. 3, pp. 2479–2481, May 2019.

[29] M. N. Ambia, K. Meng, W. Xiao, A. Al-Durra, and Z. Y. Dong, "Interactive grid synchronization-based virtual synchronous generator control scheme on weak grid integration," *IEEE Trans. Smart Grid*, vol. 13, no. 5, pp. 4057–4071, Sep. 2022.

[30] L. Huang, H. Xin, and F. Dörfler, "$\mathcal{H}_\infty$-control of grid-connected converters: Design, objectives and decentralized stability certificates," *IEEE Trans. Smart Grid*, vol. 11, no. 5, pp. 3805–3816, Sep. 2020.

[31] K. Ogata, *Modern Control Engineering*. Prentice Hall, 2009.

[32] M. Chen, D. Zhou, and F. Blaabjerg, "Power control of grid-forming converters based on full-state feedback," in *IECON 2022 – 48th Annu. Conf. IEEE Ind. Electron. Soc.*, pp. 1–6.

[33] R. C. Dorf and R. H. Bishop, *Modern Control Systems*. Prentice Hall, 2010.

[34] C.-T. Chen, *Linear System Theory and Design*. Oxford University Press, 1999.

[35] M. S. Bhatt, "Short circuit studies and relay coordination of an IEEE 14-bus power system network using ETAP," Master's thesis, California State University, Northridge, Dec. 2010.

[36] S. Dong and C. Chen, "Analysis of feasible synchronverter pole-placement region to facilitate parameter tuning," *IEEE Trans. Energy Convers.*, vol. 36, no. 4, pp. 2782–2793, Dec. 2021.